Progress In Electromagnetics Research, PIER 8, 299–348, 1994

FINITE ELEMENT SOLUTION OF THE ATMOSPHERE'S ELECTROMAGNETIC RESPONSE TO CHARGE PERTURBATIONS ASSOCIATED WITH LIGHTING

M. E. Baginski

1. Introduction

1.1 Opening Remarks

Mankind has for generations marveled at the natural phenomena of lightning. Little, however, was actually known about its true nature until Benjamin Franklin experimentally determined that it consisted of electrical charge being displaced. Following Franklin's pioneering work, the next major advances in understanding lightning took place around the year 1920 by Wilson, 1916 [1]; Watson and Craib, 1920 [2]; Appleton, 1920 [3]. During this period, increasing numbers of scientists began to investigate the fundamental reason for lightning's existence and behavior. This investigation has steadily grown and continues today with large numbers of researchers considering the thermodynamic, chemical and electrical mechanisms involved.

The study of the middle atmosphere's electrical response to lightning has been limited in the past by insufficient observations. Models developed to describe this region have therefore relied heavily on the use of assumptions [4] and have not undergone the test of agreement with data. Electrical measurements in this region, however, are slowly but surely being made available and, at least for some cases, exhibit behaviors different from conventional theoretical predictions [5]. This fact was the primary reason the present investigation was undertaken. The study to be described analyzes the atmosphere's electrical behavior using a computer solution of the general set of Maxwell's equations without constraining the electric field to be conservative ($\overline{E} = -\nabla\phi$ is not assumed). What follows are two sections describing qualitatively what occurs in a thunderstorm accompanied by a brief historical review.

1.2 The Thunderstorm

Thunderstorms and thunderclouds are usually created in an environment containing cold, dense air above warm, humid air. The warm air ascends in updrafts and forms clouds as water vapor condenses out while the cold air aloft descends. Such conditions ordinarily occur when the earth is heated by the sun's rays causing the air adjacent to the earth's surface to become strongly heated.

Thunderclouds have a large variation in size, ranging from the small clouds seen in semi-tropical storms to very immense clouds com-

mon at American Midwestern storm systems [4]. Some of the larger storm clouds reach altitudes exceeding 20 km; however, the height of a typical thundercloud is usually thought to be less than 12 km [6]. Actually the word typical should only be used for a given geographic location in that the location determines what is typical. Within a "typical" thunderstorm, there is a turmoil of wind, water vapor, water drops, and ice crystals acted upon by gravity, large temperature gradients and electric fields [7]. The forces interact with the constituents of the thundercloud by mechanisms not fully understood and generate charged regions within the thundercloud. The upper part of the thundercloud is composed of positive charge with the lower part containing a net negative charge [8]. The geometry of the thundercloud becomes one of an electric dipole. The charged sections of the thundercloud are of the order of kilometers in diameter [6] and for simplicity are represented as spheres in most models [9]. In addition to this large dipole representation, there may also be a small amount of positive charge at the base of the thundercloud. Figure 1.1 shows a schematic diagram for the probable distribution of charge in a South African thunderstorm including the small positive base charge [6]. The small positive charge plays a role in shaping the electric field structure immediately within its confines, but at altitudes of interest to this research (30–40 km) it has a negligible effect and will not be included as a modeling variable.

The lightning that occurs in a thunderstorm is a result of localized charge build up sufficient to cause electrical breakdown of the atmosphere. Each cloud-to-ground stroke begins with a weakly luminous predischarge, the leader process [6], which usually propagates from cloud-to-ground and which is followed by a very luminous return stroke. The return stroke usually propagates from ground to cloud. The predischarge initiating the lightning is given the name stepped leader because it appears to move downward in luminous steps of typically 50-meter length with a time delay between steps of approximately 50 microseconds.

Once the stepped leader has neared the ground, the resulting high electric field is sufficient to cause an upward-moving discharge from the ground to the leader tip. When this connection is made, the return stroke begins. The return stroke current typically rises to 10 to 20 kiloamperes in a few microseconds and falls to one-half of the peak value in 20 to 100 microseconds [6]. Currents of the order of hundreds of amperes may continue to flow for several hundred microseconds.

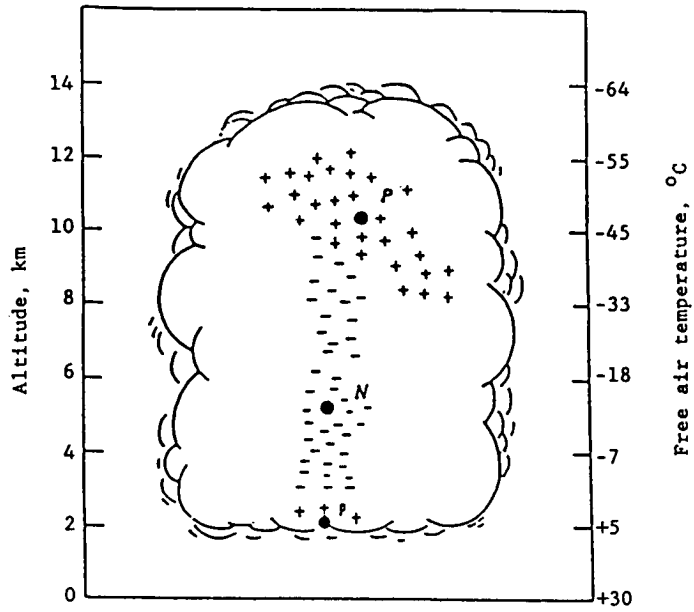

Figure 1.1 Probable distribution of thundercloud charges P, N, and p for a South African thundercloud according to Malan (1952).

Intracloud discharges occur between the upper positive and lower negative charge centers. It is thought that the intracloud discharge is very similar to the cloud-to-ground flash in that a propagating leader bridges the gap between the charge centers followed by a high intensity return stroke [6]. The total charge neutralized in an intracloud discharge is the same order of magnitude as the charge transferred in a cloud-to-ground discharge.

Historical Perspective

Since the 1950's several electrical models describing the interaction of thunderstorms with the atmosphere have been published. The research groups responsible for this work and for the shaping of scientific opinion on this subject, over the past 25 years, are rather few in number. Holzer and Saxon have assumed concentrated charges in a dipole configuration with spatially varying conductivities to obtain temporally invariant electric field patterns in the lower atmosphere and ionosphere. The lightning return stroke, however, generates transients in the observed electrical field known as "field changes" [6]. Early work-

ers attributed this temporal recovery to recharging within the thundercloud. Tamura [10] is credited as the first to note that the surrounding atmosphere is also involved. He defined solutions based on the conservative electric field assumption (i.e., $\overline{\nabla} \times \overline{E} = 0$, $E \sim \overline{E}_0 \exp(-t/\tau)$, $\tau = \epsilon_0/\sigma$) that depend on the conductivity at the point of observation. Kasemir [11] constructed the first dynamic model of the thundercloud system using resistors, a capacitor, and a spark gap. His model connected a current generator, a resistor, and a capacitor in parallel to model the cloud ionospheric connections with the path to earth replaced by a resistor. More dynamic models began to follow. Anderson and Freier [12] incorporated dynamic changes in dipole charge structure with spatially varying conductivities. However, Anderson and Freier omit the total set of Maxwell's equations and a dynamic forcing current in their modeling–only the quasi-static relaxation is included.

Additional transient solutions were developed based on the "monopole" model of C. T. R. Wilson by Illingworth [13], Park and Dejnakarintra [14], Greifinger and Greifinger [15], and Holzworth and Chiu [5]. Although these four models represent significant progress toward a concise and accurate description of the lightning event, they are all deficient for calculating upper atmosphere fields and currents for the time scales of interest (i.e., $10^{-3} - 10$ seconds).

The final model discussed is Nisbet's [16] computer simulation of the dynamic development of a thunderstorm. His model segments the atmosphere into regions consisting of capacitors, resistors, current sources, and switches, whose function is to simulate electrical breakdown of the atmosphere. This is the only model available to date which allows a complete cycle of simulated lightning to occur a large number of times, thereby examining the thunderstorm's long-term properties. The model is based on the conservative field approximations ($\overline{E} = -\nabla\phi$) and therefore neglects the magnetic field's influence on the atmosphere's electrodynamic system response. The mathematical consequences associated with using the conservative field approximation will be discussed in a later section.

All of the previously discussed models provide insight into the lightning phenomenon. However, there still remains a significant number of electric field measurements [5] that these models cannot explain. Further modeling studies are therefore required that can account for these discrepancies.

2. The Model

2.1 Purpose of the Study

The purpose of this study is to investigate and produce qualitative simulations of the atmosphere's electrodynamic response to charge perturbations associated with lightning and lightning like phenomena (possibly thermonuclear detonations, i.e., the E.M.P. response) for various conductivity profiles using the complete set of Maxwell's equations. The use of the complete set of Maxwell's equations to compute the electrodynamic response of the atmosphere to simulate lightning-like charge perturbations has never been attempted and is the novelty of this work. The principal motivation for this study is the lack of agreement between models (including all lightning models reviewed earlier) and recently published electric field measurements [5].

This study uses a computer program (TWODEPEP) [28] supplied by IMSL to solve the partial differential equations governing the electromagnetic response of the atmosphere to charge perturbations. A complete description of the computer code used and its operation is provided in Appendix A. The scope of the investigation does not include the atmosphere' s response to the high current lightning transient (i.e., propagating electromagnetic energy induced by the lightning return stroke's current) and addresses the electrodynamics immediately following the lightning column's cessation.

A very wide range of possible electrical parameters must be considered when constructing a realistic model of the thunderstorm system. The variables chosen for this research include three altitude-varying conductivities and both monopole and dipole charge configurations . The temporal structure of the electric fields is investigated for altitudes of 30–40 km and radial distances of 0–30 km. A special effort is made to identify unusual behavior in the simulations that may then be investigated via experimental techniques.

The lightning event is modeled in terms of charge perturbations located at typical altitudes of upper and lower thunderstorm charge centers. This type of lightning model has been widely used when analyzing the middle and upper atmosphere's electrical field recovery following lightning [17].

Since only the non-propagating portion of the lightning return stroke is investigated in this study, the amount of charge reduced in

the thundercloud during the lightning discharge is used as the input parameter for the model for both cloud-to-ground and intracloud lightning.

In cloud-to-ground lightning, there exists a large negative lower charge center that is reduced in magnitude following the lightning event. This is conveniently modeled by applying the equivalence principle and introducing a positive charge into the center thereby reducing the amount of negative charge in the lower center [9]. The charge introduced during the cloud-to-ground lightning has a spherical Gaussian profile and is centered about the z-axis at the height of the lower negative charge and will be referred to as a monopole of charge in later sections.

The modeling of intracloud lightning is done in a similar fashion. A negative charge of identical magnitude and temporal characteristics as the positive charge perturbation is introduced at the center of the upper charge. By superimposing the resultant responses of both the intracloud and the cloud-to-ground simulations the intracloud response is simulated. Since the simulations consist of two charge centers, the corresponding responses will be identified as those of a *dipole*. A single charge perturbation at either altitude is shown in Figure 1.2; this may be described mathematically as follows:

$$Q_f(t) = \int_0^t i_R(t)dt$$

where

$i_R(t)$ =lightning return stroke current
$Q_f(t)$ =total displaced charge of the return stroke

The specifics of the introduction of the charges are discussed in a later section and in Appendix A.

It is important to note that only the transient portion of the late-time electric field recovery following lightning is considered here.

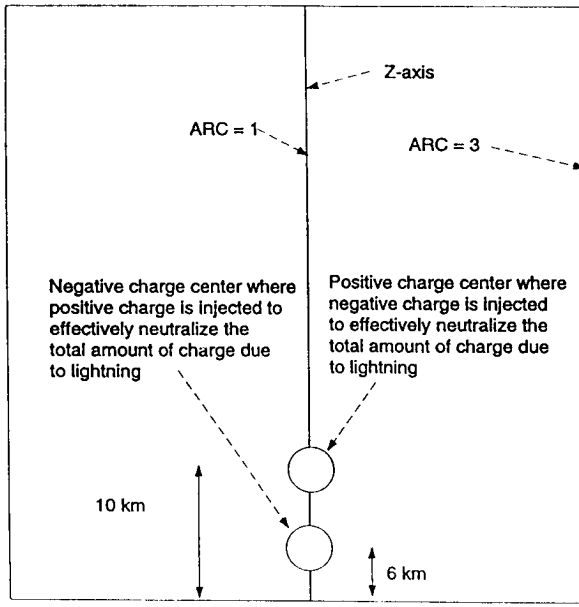

Figure 1.2 Boundaries used for the electrical model of the atmosphere with charge injection shown.

2.2 Discussion of the Model

Charging mechanisms

In thunderstorm research the most difficult phenomena to explain have been the processes involved in cloud electrification. The difficulty is twofold: on the one hand, there are a large number of possible mechanisms responsible for charge separation and current generation; while on the other hand, it is usually impossible to isolate such mechanisms and test each for its relative effect. Regardless of the mechanisms, what is known is that a thunderstorm is sustained by charge separation which can be approximated by net positive and negative charge centers. The height of the charge centers is somewhat affected by seasonal changes and the geographic location. Typical heights of 10 km for the upper charge center and 6 km for the lower charge center are widely found in the literature and have been selected for this research [18].

The magnitudes and profiles of the charge centers and currents

vary significantly from storm to storm. Kasemir, for instance, has measured values ranging from 20 coulombs up to 1000 coulombs for thundercloud charges and cloud electrification currents from less than 0.1 ampere to 10 amperes. Lightning return stroke currents are reported to have an even larger range of values. The existence of such large variations complicates selection of the currents and the charge deposition profile. After a review of the relevant literature, a judicious choice of the forcing current and profile of charge deposition was made. The charge perturbation used was developed based on Sunde's [19] lightning return stroke current model.

It is well known that the deposition of the return stroke current is primarily responsible for the charge perturbation. The deposition rate of the lightning return stroke current is proportional to the time derivative of the charge perturbation. Therefore, the total charge deposited at time t may be expressed as the integral of the lightning return stroke current in time (i.e., time history of the induced charge).

$$Q(t) = \int_0^t i_R(t)dt$$

where

$i_R(t)$ = lightning return stroke current

$Q(t)$ = total displaced charge of the return stroke

Sunde's [19] lightning return stroke model is selected for the research primarily because of its extensive commercial and military use in work requiring an analytic formulation of the lightning return stroke current. This model was developed based on the statistics of a very large number of measurements compared to some but includes the fundamental attributes necessary to predict "average" electromagnetic field behavior. The charge generation (in units of amperes or coulombs /second) may be expressed in terms of this current temporally as follows:

$$i(t) = I_0(\exp(-at) - \exp(-bt))$$

$i(t)$ = lightning return stroke current (Sunde's model)

where

$a = 10^4$ seconds^{-1}

$b = 0.5 \times 10$ seconds^{-1}

I_0 = proportional to amount of charge displaced during return stroke.

The temporal structure of the forced charge generator is given as:

$\partial Q(t)/\partial t = I_0(\exp(-at) - \exp(-bt))$
$\partial Q(t)/\partial t$ is identical to G_s used in section 2.3 Maxwell's Equations.

The term $\exp(-bt)$ controls the rise time of the charge generation inducing the perturbation, i.e., how rapidly the maximum return stroke current, but not charge deposited, is attained. Since the amount of charge exchanged during a return stroke is related to its time integration, omitting the term causes no appreciable change (for times greater than 5×10^6 seconds) in the amount of charge displaced, and therefore, no appreciable change in the simulated electrodynamic response. The spatial structure of the deposited charge is given by a modified spherical Gaussian profile:

$$\frac{\partial(\rho_d(r,z))}{\partial t} = \frac{\exp(-R/2\lambda)}{(2\pi\lambda)^{1.5}}$$

where

ρ_d = deposited charge perturbation
λ = variance
$R = r^2 + (z - z')^2$
z' = altitude of charge perturbation

The spatial distribution of the charge perturbation does not noticeably affect electric field signatures far from its interior [17]. This condition exists for our model (electric fields of interest are at least 20 km from the charge perturbation) and allows a certain degree of freedom in the specification of the distribution. Also, since virtually no published data is available describing the spatial structure of the deposition of the lightning return stroke current, the selection is even more arbitrary. The modified Gaussian distribution is used in the modeling of many man-made and naturally occurring forced charge events and so was chosen for this model [20].

The numerical formulation of the charge perturbation is listed (FORTRAN statements) with comments in Appendix A. A total charge of one (1) coulomb is induced in all simulations ($1\text{C} = \int[\partial Q/\partial t]dt$) with the initial conditions being that no charge or electric field is present prior to the first time step.

2.3 Geometry of the Region

Before describing the geometry, consider again the phenomenon of interest: charge perturbations located at altitudes no greater than approximately 10 km, induce electric fields throughout the atmosphere, but only those fields induced within the middle atmosphere are to be simulated. Therefore, the model constructed must meet two criteria:

1) If not obviously constrained, the geometrical limits of the model will approximate the entire atmosphere's electrical effect on the regions where the simulations take place.

2) The boundary conditions of the region will be electrically equivalent to those of the atmosphere.

The region selected (Fig. 2.1) is contained within a perfectly conducting right circular cylinder with a radius of 60 km. A discussion of how each of the boundaries was arrived at follows:

Lower Plate—The earth's surface is electrically modeled as a perfect conductor. This assumption is based on the very large difference that exists between the earth's conductivity and adjacent atmosphere's conductivity. Typical values of 10^{-3} to 10^{-2} mhos/meter [9] are given for the earth's conductivity, while 10^{-14} to 10^{-13} mhos/meter is the usual range of the adjacent atmosphere's conductivity. This difference of more than 11 orders of magnitude makes the earth appear (electrically) as a perfect conductor. This assumption is commonly used in practical antenna engineering for frequencies whose range would correspond to time scales of 10^{-9} to 10^{+1} seconds [21], ranges well beyond the maximum and minimum time scales of this research (Minimum time step used in the research is 5×10^{-6} seconds with a total duration of 4 seconds.)

Upper Plate—The selection of 80 km for the height of the upper boundary was a necessary consequence of the atmospheric conductivity structure being complicated by the Hall and Pederast components above an altitude of approximately 70 km [17]. The tensor conductivity components result when the mean free path and velocities of the charge carriers are sufficient to allow their trajectories to be altered by the effect of the earth's magnetic field [22]. The finite element routine employed in the solution is not capable of modeling tensor conductivities; therefore, an altitude limit must be set in the vicinity of 70 km.

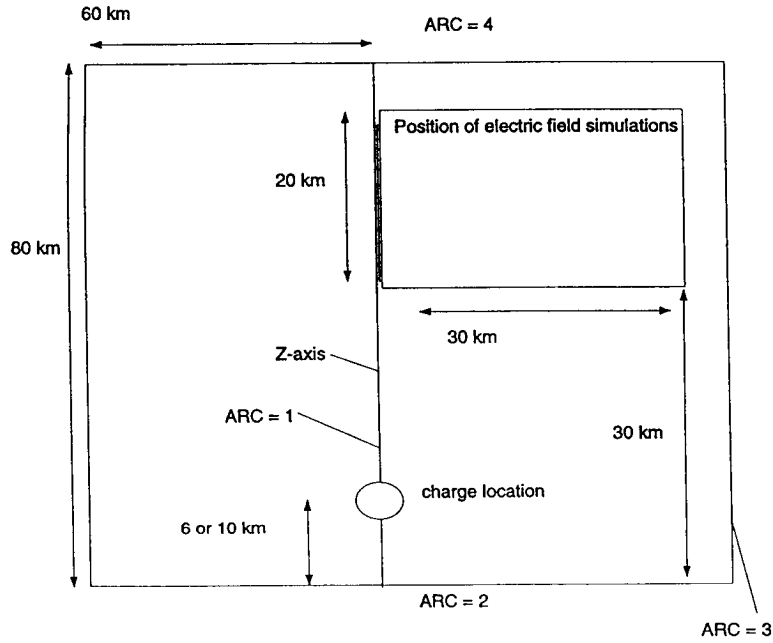

Figure 2.1 Boundaries used for the electrical model of the atmosphere.

The 80-km altitude was selected based on the following considerations:

1) The relative magnitude of these two tensor conductivity components is approximately proportional to the additional distance in altitude (beyond 70 km) considered. The maximum value of either of these components with respect to the parallel conductivity's magnitude (for the range of altitudes considered) is less than 10 percent [9].

2) The middle and upper atmospheric electric fields resulting from lightning (with the exception of the $\sim 10^{-4}$ second propagating component) are approximately vertically oriented i.e., the horizontal component is negligible.

3) The off-diagonal tensor components of the high-altitude conductivity only interact with electric fields that are not aligned with the earth's magnetic field. Since the earth's magnetic field, with the exception of the equatorial regions, is primarily vertically aligned, the influence of both the Pederson and Hall components on the lightning-induced vertical electric fields will be, to first order, negligible.

An obvious concern is the influence this 80-km altitude limit

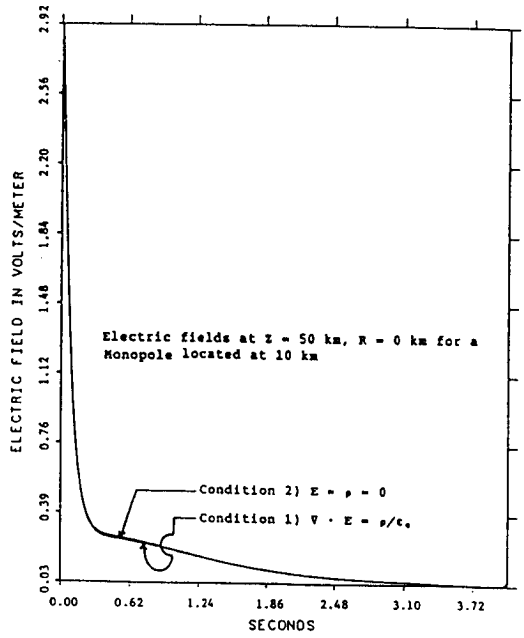

Figure 2.2 Effects of the Upper Plate being set to: 1) $\nabla \cdot \overline{E} = \rho/\epsilon$. 2) $\overline{E} = \rho = 0$.

may have on the simulations. To investigate the maximum possible error (assuming an electrically passive ionosphere) that this would introduce in the solutions, two sets of simulations were done with the 80-km upper plate electrically described by: 1) The vertical electrical field and charge density are set to a value of zero ($\overline{E} = \rho = 0$). 2) The divergence of the electric field is set to the value of the charge density divided by the permittivity of free space ($\nabla \cdot \overline{E} = \rho/\epsilon_0$). When results were compared, little, if any, difference could be seen for the time frames of interest (0–4 seconds) in any of the cases (all cases were subject to this test). The largest difference occurred for the simulation done using the exponential conductivity with charge perturbation located at 10 km (Fig. 2.2), indicating that the simulations were relatively insensitive to the boundary conditions at an altitude of 80 km (outer cylindrical boundary of 60 km was used in all cases).

The probable reason for this behavior is that in general, for light -ning-induced transients, the electrical properties of the atmosphere below the point of observation of the field rather than above, govern the

transients' response. This may be explained by simply considering the fact that, in general, the conductivity (true for all conductivities used in this study) rapidly increases with altitude (i.e., resistivity decreasing), and therefore its influence (restrictive effect) on total global charge movement decreases. Hence, it seems reasonable to assume the middle atmosphere' s simulated response to low-altitude charge perturbations is governed by the adjacent and lower altitude conductivity values.

Outer Cylindrical Surface—The lateral boundary had no distance constraint and could have been extended indefinitely. However there exists a trade-off between accuracy and resolution: the smaller the model dimensions the greater the accuracy in solving the differential equations. Therefore, the errors resulting from the adoption of finite boundaries for the model must be weighed against those resulting from degrading the numerical resolution of TWODEPEP by involving too large a volume.

The simulations were found to be insensitive to increases in the radial limit beyond 50 km for all cases. No visible difference could be detected in the responses using either 50-km or 60-km radial boundaries when plotted together (comparative plot not included). Therefore, selecting a 60-km radial limit is a measure taken to provide additional confidence in the simulations.

Axis of Symmetry (z-axis)—Since $r = 0$ defines an axis of symmetry and since there are no discontinuities in the charge distribution, the derivative of the vertical electric field $(\partial E_z/\partial r)$ with respect to radial distance reduces to zero on this axis.

The differential forms of the four boundary conditions are summarized as follows:

1) At ARC $= +1$ (z-axis), $(\partial E_z/\partial r) = 0$.
2) At ARC $+2, +4$ (upper and lower boundaries).

$$\nabla \cdot \overline{E} = \rho/\epsilon_0, E_r = 0$$

3) At ARC $= -3$ (outer radial boundary), $\rho = E_z = 0$.

2.4 Conductivities

The three altitude-varying conductivity profiles selected for comparison (Fig. 2.3) are the Gish [7] model, and exponentially-varying

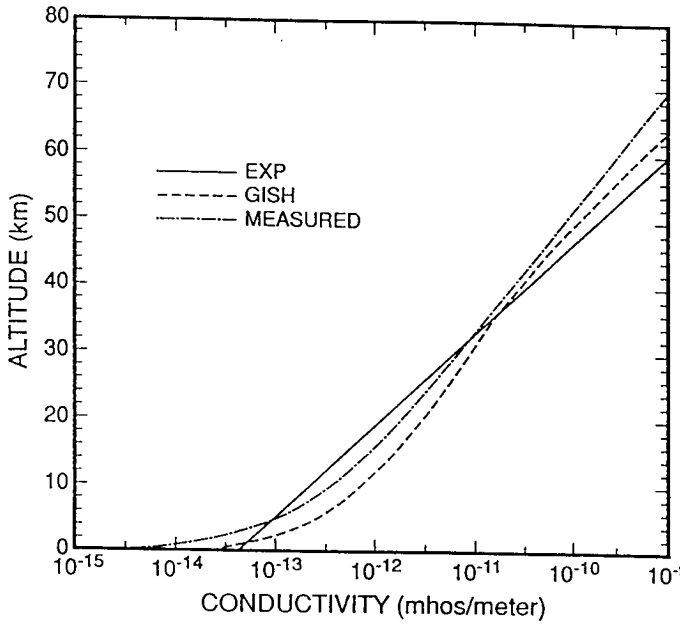

Figure 2.3 The Conductivities.

conductivity $[5 \times 10^{-14} \exp(Z/6000 \text{ m})$ mho/m], and a profile constructed based on data obtained during a thunderstorm campaign on 8 August, 1981, conducted at Wallops Island Virginia [23]. The Gish and the exponentially-varying conductivities are both widely used in atmospheric electrical models [13]. The Gish conductivity has a greater rate of change versus altitude and a wider range of values than the exponential. This difference provides a measure to correlate with the resulting field simulations. The third conductivity profile, approximating the measurements, displays and even greater rate of change and range of values than the Gish profile, and therefore extends the possible correlation. This third profile is based on measurements and will be referred to as the REAL conductivity in the following discussions for simplicity. It is believed that the three conductivity profiles are representative of the conductivities in the (nighttime) mid-latitude atmosphere.

2.5 Maxwell's Equations

To those familiar with classical electromagnetics, the analysis of

the post-stroke atmospheric response may appear relatively simple at first. A charge imbalance induced in a conducting region would be expected to decay exponentially with time at a rate determined by the local relaxation time of the region. The corresponding electric fields, being proportional to the overall charge distribution, would also be expected to decay in this manner. When electric field measurements obtained from parachute-borne payloads [24] are considered, however, a significant deviation from the exponential decay is at times observed. In some cases a gradual peaking is observed hundreds of milliseconds after the return stroke has ceased. This behavior suggests, at least for some circumstances, that a more complicated description is required and that a careful analysis of the governing equations should be undertaken.

Beginning with Maxwell's equations, a single equation is derived where the electric field is dependent on the charge density only as follows:

$$\overline{\nabla} \times \overline{E} = -\mu_0 \partial \overline{H}/\partial t \tag{2.2}$$

$$\overline{\nabla} \times \overline{H} = \overline{J} + \partial \overline{D}/\partial t + \text{any additional sources of charge movement} \tag{2.3}$$

$$\nabla \cdot \overline{D} = \rho \tag{2.4}$$

$$\nabla \cdot \overline{H} = 0 \tag{2.5}$$

$$\overline{J} = \sigma \overline{E} \tag{2.6}$$

$$\overline{D} = \epsilon_0 \overline{E} \tag{2.7}$$

The wave equation is developed using the above equations as follows:

1) taking the curl (2.2)

$$\overline{\nabla} \times \overline{\nabla} \times \overline{E} = -\mu_0 \partial(\nabla \times \overline{H})/\partial t \tag{2.8}$$

2) using the vector identity

$$\overline{\nabla} \times \overline{\nabla} \times \overline{E} = \nabla \nabla \cdot \overline{E} - \nabla^2 \overline{E}$$

3) substituting (2.3) for $\nabla \times \overline{H}$ in (2.8)

4) substituting (2.4), (2.6), (2.7) in (2.8) results in the wave equation

$$\overline{\nabla} \times \overline{\nabla} \times \overline{E} = -\mu_0 \sigma \partial \overline{E}/\partial t - \mu_0 \epsilon_0 \partial^2 \overline{E}/\partial t^2 \tag{2.9}$$

or

$$\nabla \rho/\epsilon_0 = \nabla^2 \overline{E} - \mu_0 \sigma \partial \overline{E}/\partial t - \mu_0 \epsilon_0 \partial^2 \overline{E}/\partial t^2 \tag{2.10}$$

The resulting second order partial differential equation (2.10) is analytically solvable for only the simplest cases. The types of solutions

required for altitude-dependent conductivities are not obvious. If one wishes to pursue this problem further, assumptions must be made or a numerical methods approach must be applied. The most common assumption used in the past is to define the electric field as the gradient of the electric potential ($E = -\nabla\phi$), the conservative field equation. The mathematical consequence of this is to constrain the electric field to decay exponentially in time. This can be shown as follows:

if $\overline{E} = -\nabla\phi$

$\overline{\nabla} \times \overline{E} = \nabla \times (-\nabla\phi) = 0$ (vector identity)

$\overline{\nabla} \times \overline{\nabla} \times \overline{E} \equiv 0$ (the curl of a constant, in this case is 0)

then (2.9) reduces to

$$0 = -\mu_0\sigma\partial\overline{E}/\partial t - \mu_0\epsilon_0\partial^2\overline{E}/\partial t^2$$

The general solution of this partial differential equation is:

$$\overline{E}(\underline{x}, t) = \overline{E}_1(\underline{x}) \exp(-t/\tau(\underline{x})) + \overline{E}_0(\underline{x})$$

where

$\underline{x}$ is a position vector in any general coordinate system

$\tau(\underline{x}) = \epsilon_0/\sigma(\underline{x})$

This type of solution has a definite range of validity. However, for the general case, a computer solution of (2.10), not limited by the conservative field assumption, would provide more information about the true time-dependent shape of the electric field.

The last equation required for the simulations is the continuity equation. This is derived by taking the divergence of (2.3) and substituting in (2.4), (2.5), (2.6), and (2.7) (the order is unimportant) as follows:

$$\begin{aligned}
&\nabla \cdot (\overline{\nabla} \times \overline{H}) = \nabla \cdot (\sigma\overline{E} + \epsilon_0\partial\overline{E}/\partial t + \overline{J}_s) \\
&\nabla \cdot (\nabla \times H) \equiv 0 \text{ (vector identity)} \\
&0 = \nabla \cdot \sigma\overline{E} + \epsilon_0\partial\overline{E}/\partial t + \overline{J}_s) \\
&0 = \nabla \cdot (\sigma\overline{E}) + \nabla \cdot (\epsilon_0\partial\overline{E}/\partial t) + (\nabla \cdot \overline{J}_s) \\
&0 = \sigma\nabla \cdot \overline{E} + \nabla\sigma \cdot \overline{E} + \epsilon_0\partial(\nabla \cdot \overline{E})/\partial t + \overline{G}_s \\
&0 = \sigma\rho/\epsilon_0 + \nabla\sigma \cdot \overline{E} + \partial\rho/\partial t + \overline{G}_s
\end{aligned} \tag{2.11}$$

where

$\overline{J}_s =$ source current inducing the charge perturbation
$\nabla \cdot \overline{J}_s = \overline{G}_s =$ source charge generator creating perturbation

Equations (2.10) and (2.11) are derived from Maxwell's equations and describe the electrodynamic response of the atmosphere to charge perturbations. They are in required input format for TWODEPEP and in Appendix A are converted to FORTRAN statements. Only the vertical component of (2.10) is investigated and, therefore, only two equations are required.

3. Electric Field Simulations

3.1 Introduction

The electric field simulations are presented in two sections. Each section contains vertical electric field simulations at nine different locations. The first section contains the atmosphere's electromagnetic response to positive monopole charge perturbations (located at 6 km and 10 km) for all three conductivity profiles. These results may be operated on linearly (using the principle of superposition and scaling) to simulate the electric fields resulting from charge perturbations of any given magnitude whose centers are located at 6 km and 10 km. This includes lightning and other similar events (possible nuclear detonations).

The second section contains vertical electric field simulations induced by dipole charge perturbations. These simulations model light -ning-induced vertical electric fields that will be compared to observations. The experimental data selected [23] measured both the conductivity and vertical electric field concurrently. However, the payload's position relative to the lightning was unknown, causing the comparison (section 4) to be more qualitative than quantitative.

Figures shown in sections 3.1 and 3.2 are identified with a heading containing the following information:

SIMULATION 1st entry - 2nd entry - 3rd entry
1st entry = altitude of charge perturbation in kilometers or DI if dipole is used

2nd entry = radial distance of simulation in kilometers from the vertical axis

3rd entry = altitude of simulation in kilometers

3.2 The Monopoles

3.2.1 Electric field simulations for a charge perturbation located at 6 km

A) $Z = 30$ km

The interesting characteristics of these simulations (Figs. 3.1–3.8) are as follows:

1) the maximum value of the electric field for all simulations occurred 100 ms or more after the forced charge perturbation had ceased.

2) The magnitude of the electric field decreases (in all cases) as the radial distance is increased.

3) The temporal structure (peak magnitude of each may be considered normalized to a value of one) of the electric field for a given conductivity is not sensitive to radial position. This seems to indicate that the electric fields are mapped horizontally at this altitude.

B) $Z = 40$ km

4) The vertical electric field waveforms reverse polarity for simulations done at $R = 0$ km, 10 km.

5) The maximum value of the electric field for all simulations occurred 30 ms or more after the forced charge perturbation had ceased. Generally, the time delay, magnitude, and duration of the $Z = 40$ km electric field simulations are less than the previously shown $Z = 30$ km simulations.

6) For simulations where $R = 20$ km and 30 km, the electric field magnitude decreases relatively rapidly (after the maximum value is reached) for times less than approximately 2 seconds. This is followed by a much slower rate of decay for the remainder of the simulation (total duration of 4 seconds).

3.2.2 Electric field simulations for charge perturbations located at 10 km

A) $Z = 30$ km

The interesting characteristics of these simulations (Figs. 3.9–3.16) are as follows:

1) The maximum value of the electric field for all simulations occurred 100 ms or more after the forced charge perturbation had ceased.

2) The magnitude of the electric field decreases (in all cases) as the radial distance is increased.

3) The temporal structure (peak magnitude of each waveform may be considered normalized to a value of one) of the electric field for a given conductivity is not sensitive to radial position. This seems to indicate that the electric fields are mapped horizontally at this altitude. These three conditions were also observed for the 6-km charge perturbation.

B) $Z = 40$ km

4) The vertical electric field waveforms did not reverse polarity for simulations done at $R = 0$ km, 10 km (a polarity reversal was noted at these positions for the charge perturbation located at 6 km).

5) The maximum value of the electric field for all simulations occurred 30 ms or more after the forced charge perturbation had ceased. Generally, the time delay, magnitude, and duration of the $Z = 40$ km electric field simulations are less than the previously shown $Z = 30$ km simulations.

6) For all cases, the magnitude of the simulated electric field decreases relatively rapidly (after the absolute maximum value is reached) for times less than approximately 2 seconds. This is followed by a much slower rate of decay for the remainder of the simulation (total duration of 4 seconds).

3.3 The Dipole

The vertical electric fields resulting from two charge perturbations of equal magnitude and opposite polarity (negative upper, positive lower) are simulated and approximate the charge displaced during and intracloud lightning discharge. The upper and lower charge perturbations are located at 10 km and 6 km respectively. The temporal and spatial structure of each is described in Section 2.2 and also in Appendix A.

All three altitude-varying conductivities are used.

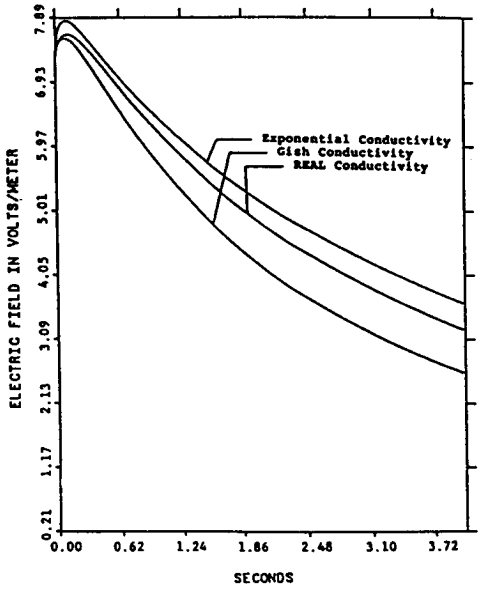

Figure 3.1 Electric field simulations at $Z = 30$ km, $R = 0$ km for a monopole of charge located at 6 km.

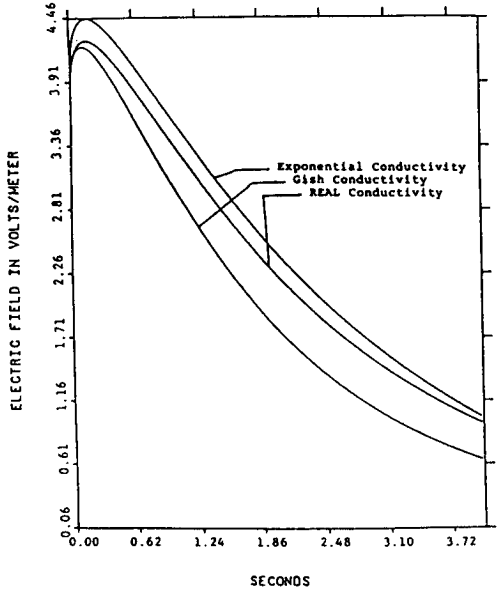

Figure 3.2 Electric field simulations at $Z = 30$ km, $R = 10$ km for a monopole of charge located at 6 km.

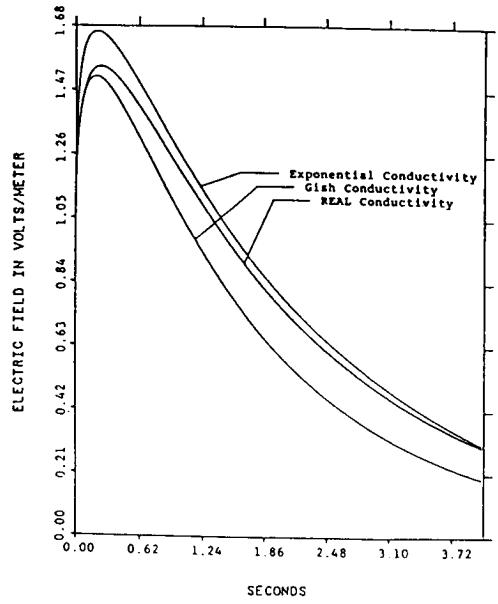

Figure 3.3 Electric field simulations at $Z = 30$ km, $R = 20$ km for a monopole of charge located at 6 km.

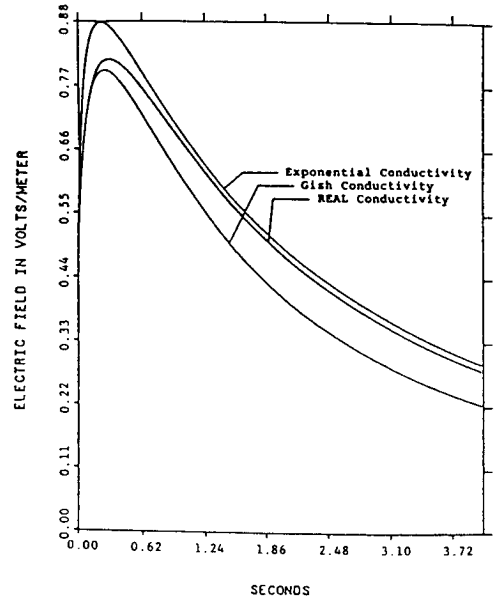

Figure 3.4 Electric field simulations at $Z = 30$ km, $R = 30$ km for a monopole of charge located at 6 km.

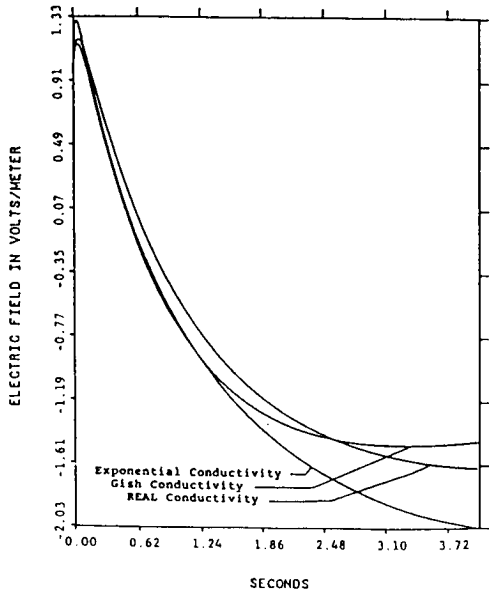

Figure 3.5 Electric field simulations at $Z = 40$ km, $R = 0$ km for a monopole of charge located at 6 km.

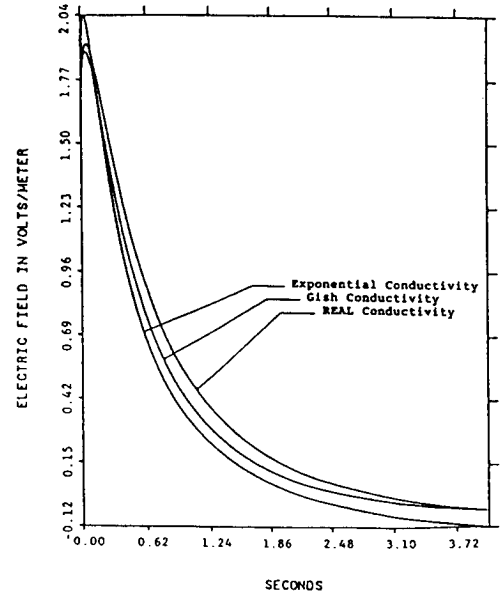

Figure 3.6 Electric field simulations at $Z = 40$ km, $R = 10$ km for a monopole of charge located at 6 km.

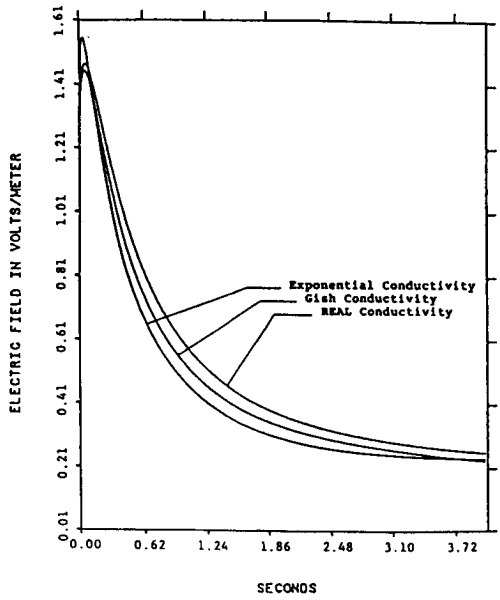

Figure 3.7 Electric field simulations at $Z = 40$ km, $R = 20$ km for a monopole of charge located at 6 km.

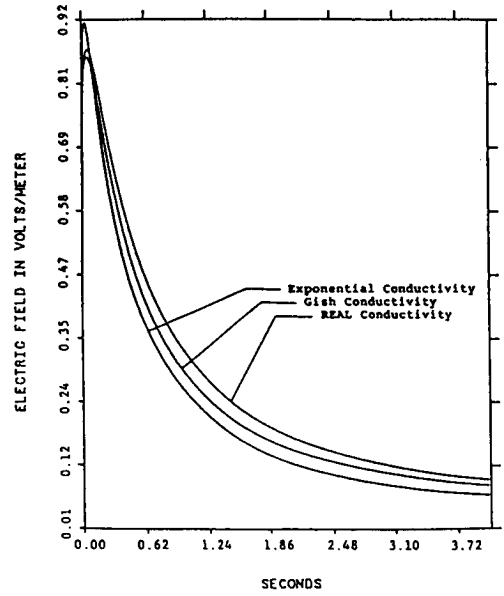

Figure 3.8 Electric field simulations at $Z = 40$ km, $R = 30$ km for a monopole of charge located at 6 km.

3.3.1 Electric field simulations for a dipole

A) $Z = 30$ km

The interesting characteristics of these simulations (Figs. 3.17–3.24) are as listed:

1) The maximum absolute value of the electric field for all simulations occurred 100 ms or more after the forced charge perturbation had ceased.

2) The absolute value of the electric field decreases (in all cases) as the radial distance is increased.

3) The temporal structure (peak magnitude of each waveform may be considered normalized to a value of one) of the electric field for a given conductivity is not highly sensitive to the radial position. This seems to indicate the electric fields are, as was the case for the monopole simulations, mapped horizontally at this altitude.

4) The electric field waveforms show (for the $R = 0$ km, 10 km, and 20 km simulations) a slight field inversion for times greater than 3.5 seconds. The maximum value of the inverted electric fields for all cases was less than twenty percent (20%) of the corresponding non-inverted electric field values.

5) Overall, there is a high degree of similarity in the temporal structure of the dipole and monopole vertical electric field simulations at this altitude.

B) $Z = 40$ km

6) The vertical electric field waveforms (for all cases) did not reverse polarity.

7) The maximum value of the electric field for all simulations occurred 30 ms or more after the forced charge perturbation had ceased. Generally, the time delay, magnitude, and duration of the $Z = 40$ km electric field simulations are less than that of the previously shown $Z = 30$ km simulations (this characteristic was observed in the corresponding monopole simulations).

8) The electric field simulations for $R = 10$ km, 20 km, and 30 km showed a high degree of similarity. However, the on-axis ($R = 0$ km) electric field simulations for the exponential conductivity varied a great deal (both temporally and in magnitude) from those of the Gish and REAL conductivities.

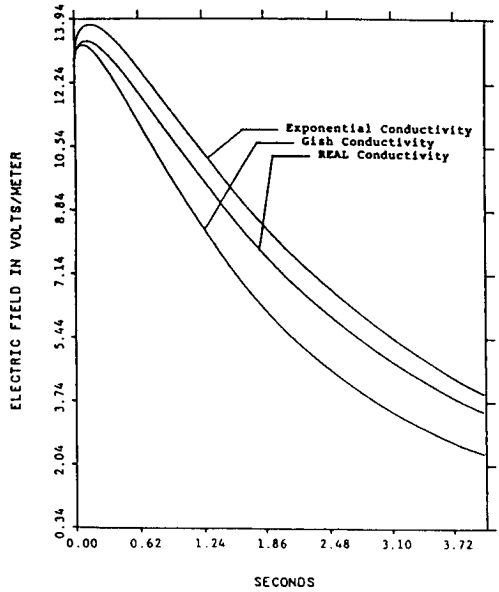

Figure 3.9 Electric field simulations at $Z = 30$ km, $R = 0$ km for a monopole of charge located at 10 km.

3.4 Spatial Distribution of the Simulated Vertical Electric Fields of Lightning

This section contrasts the vertical and horizontal (distance) dependence of the simulated vertical electric fields corresponding to intracloud and cloud-to-ground lightning (Figs. 3.25–3.28). The altitude variation is displayed by superimposing the vertical electric field simulations for the on-axis ($R = 0$ km) cases at altitudes of 30 km, 40 km, and 50 km. The horizontal dependence is likewise shown by superimposing the vertical electric field simulations at a altitude of 30 km for radial distances of 0 km, 10 km, 20 km, and 30 km.

There are two general characteristics that can be identified in these comparisons:

1) The initial rise time and early-time rate of decay the electric field simulations increases as altitude is increased.

2) The magnitude of the vertical electric field simulations decreases as radial distance is increased, while the temporal structure remains relatively unaffected.

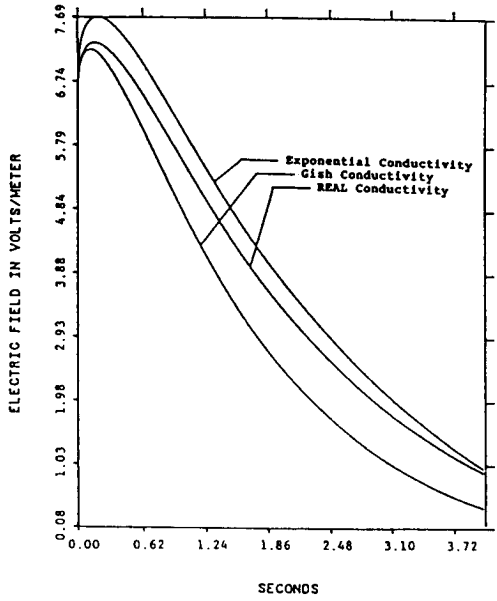

Figure 3.10 Electric field simulations at $Z = 30$ km, $R = 10$ km for a monopole of charge located at 10 km.

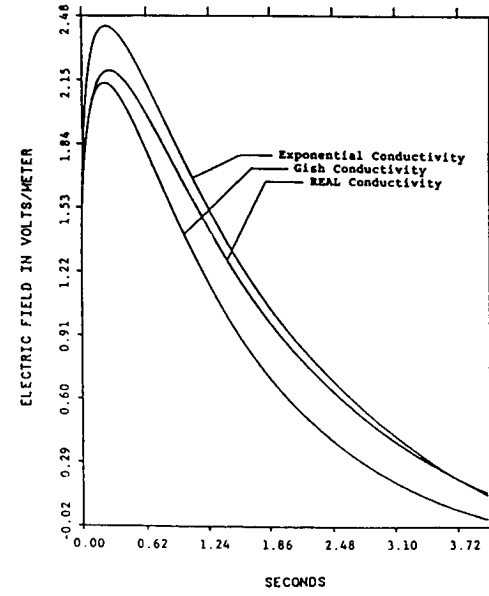

Figure 3.11 Electric field simulations at $Z = 30$ km, $R = 20$ km for a monopole of charge located at 10 km.

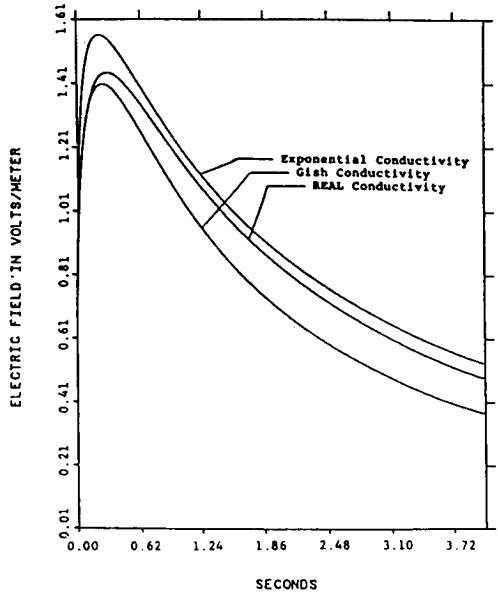

Figure 3.12 Electric field simulations at $Z = 30$ km, $R = 30$ km for a monopole of charge located at 10 km.

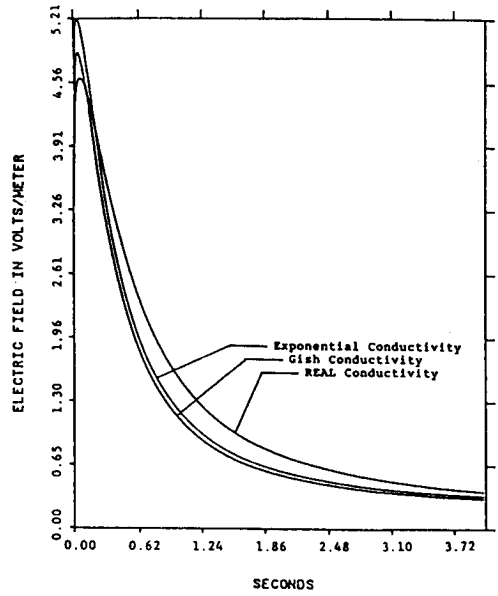

Figure 3.13 Electric field simulations at $Z = 40$ km, $R = 0$ km for a monopole of charge located at 10 km.

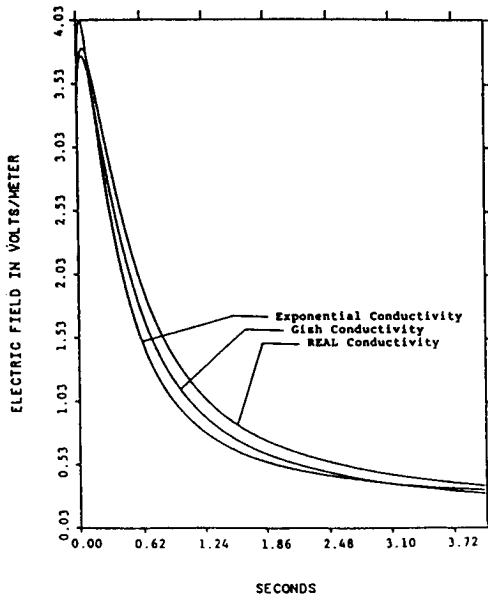

Figure 3.14 Electric field simulations at $Z = 40$ km, $R = 10$ km for a monopole of charge located at 10 km.

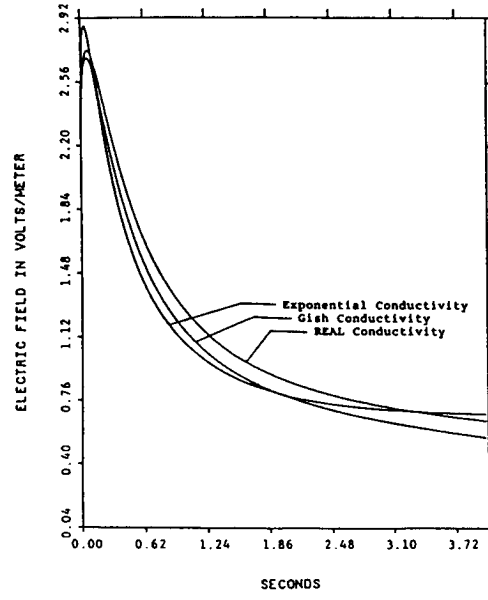

Figure 3.15 Electric field simulations at $Z = 40$ km, $R = 20$ km for a monopole of charge located at 10 km.

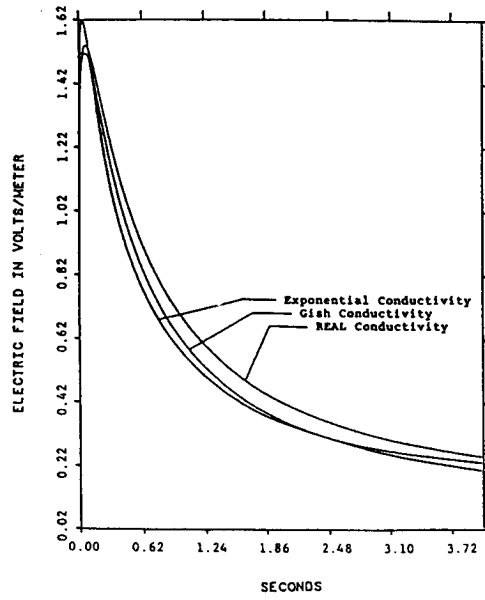

Figure 3.16 Electric field simulations at $Z = 40$ km, $R = 30$ km for a monopole of charge located at 10 km.

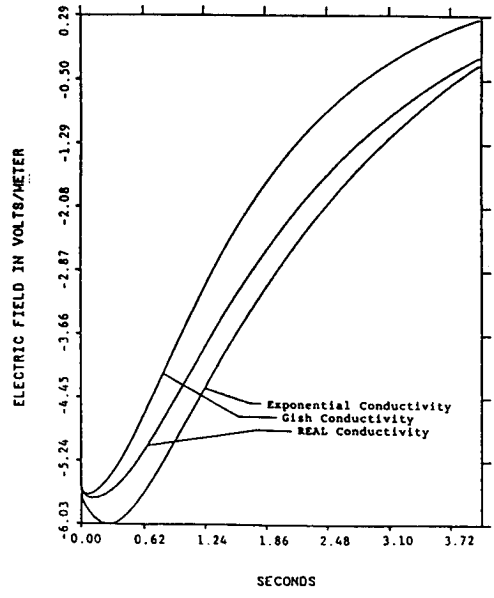

Figure 3.17 Electric field simulations at $Z = 30$ km, $R = 0$ km for a dipole with $(-)$ 10 km upper charge and $(+)$ 6 km lower charge simulating intracloud lightning.

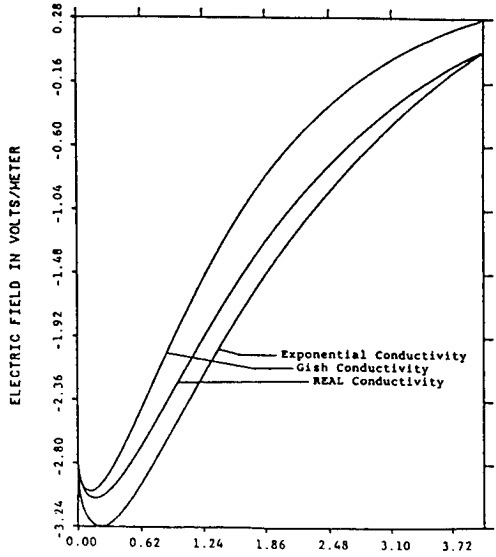

Figure 3.18 Electric field simulations at $Z = 30$ km, $R = 10$ km for a dipole with $(-)$ 10 km upper charge and $(+)$ 6 km lower charge simulating intracloud lightning.

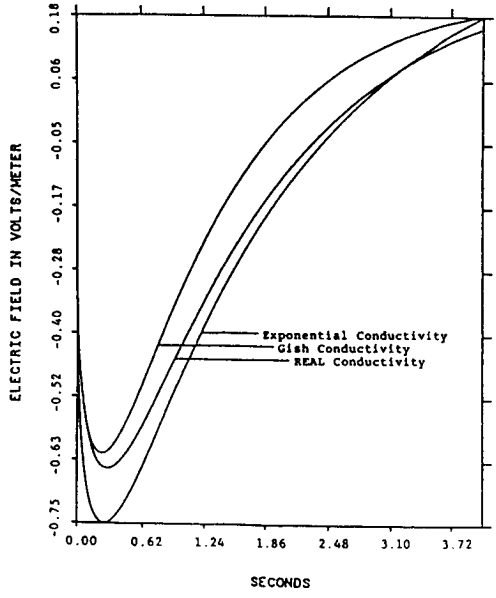

Figure 3.19 Electric field simulations at $Z = 30$ km, $R = 20$ km for a dipole with $(-)$ 10 km upper charge and $(+)$ 6 km lower charge simulating intracloud lightning.

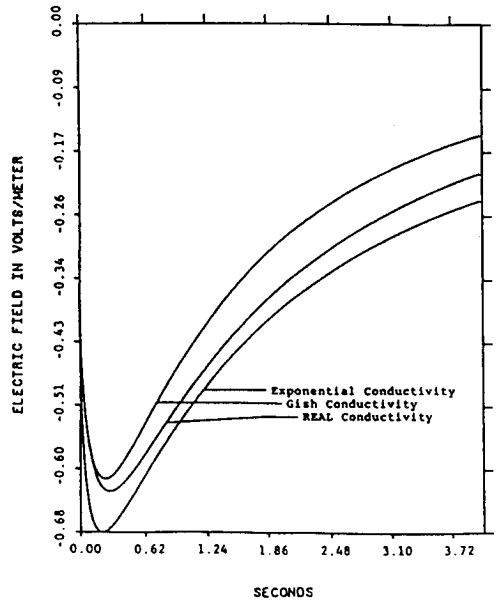

Figure 3.20 Electric field simulations at $Z = 30$ km, $R = 30$ km for a dipole with $(-)$ 10 km upper charge and $(+)$ 6 km lower charge simulating intracloud lightning.

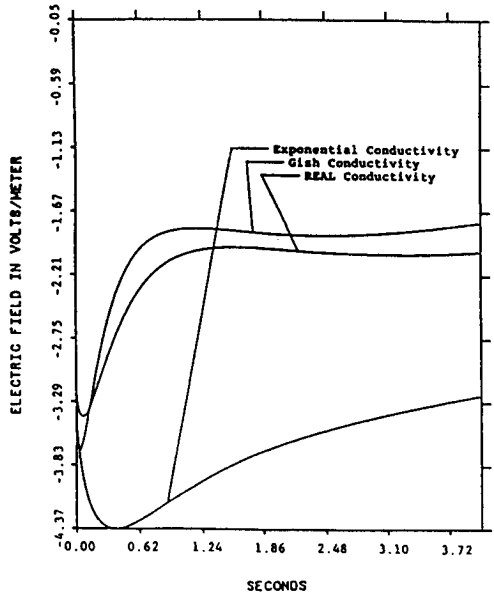

Figure 3.21 Electric field simulations at $Z = 40$ km, $R = 0$ km for a dipole with $(-)$ 10 km upper charge and $(+)$ 6 km lower charge simulating intracloud lightning.

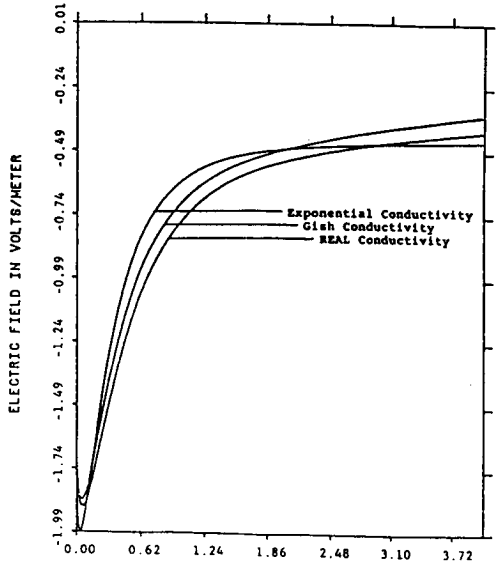

Figure 3.22 Electric field simulations at $Z = 40$ km, $R = 10$ km for a dipole with $(-)$ 10 km upper charge and $(+)$ 6 km lower charge simulating intracloud lightning.

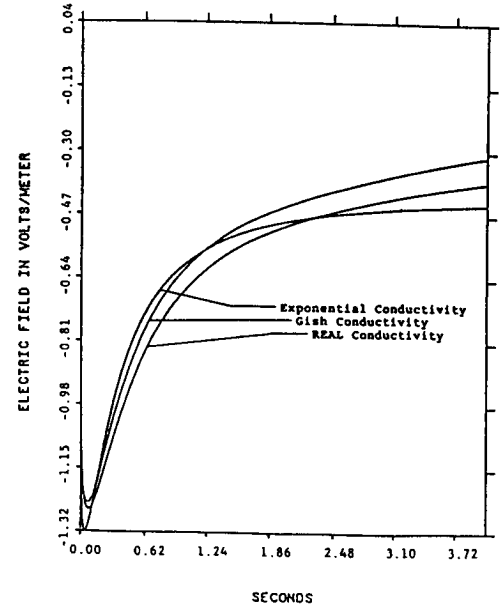

Figure 3.23 Electric field simulations at $Z = 40$ km, $R = 20$ km for a dipole with $(-)$ 10 km upper charge and $(+)$ 6 km lower charge simulating intracloud lightning.

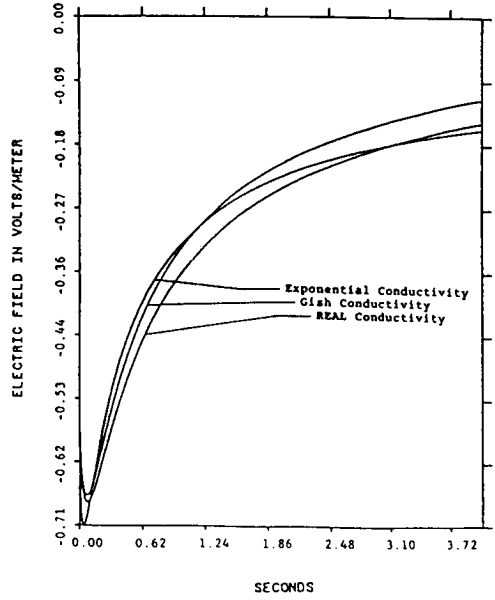

Figure 3.24 Electric field simulations at $Z = 40$ km, $R = 30$ km for a dipole with $(-)$ 10 km upper charge and $(+)$ 6 km lower charge simulating intracloud lightning.

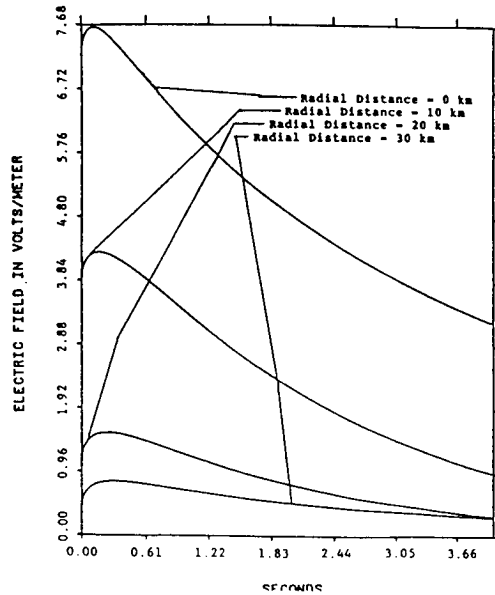

Figure 3.25 Radial distribution of simulated electric fields at $Z = 30$ km for a monopole located at 6 km using real conductivity.

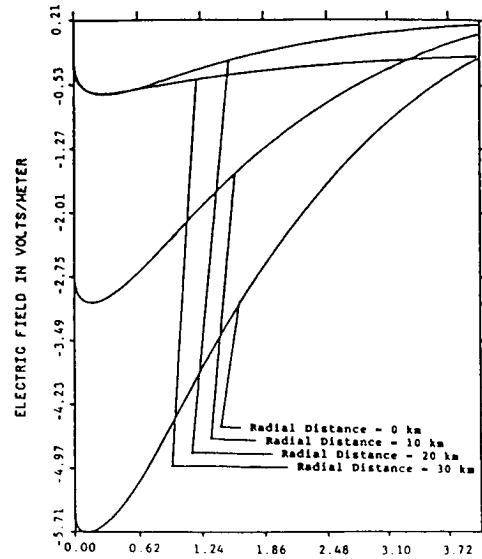

Figure 3.26 Radial distribution of simulated electric fields at $Z = 30$ km for a dipole with $(-)$ 10 km upper and $(+)$ 6 km lower charge centers using real conductivity.

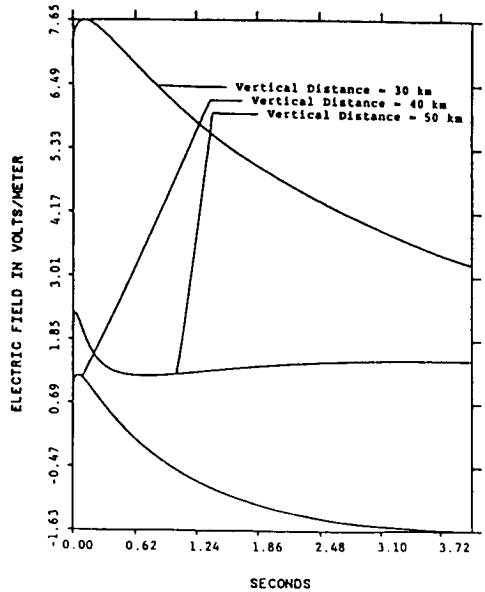

Figure 3.27 Vertical distribution of simulated electric fields at $Z = 30$ km for a monopole located at 6 km using real conductivity.

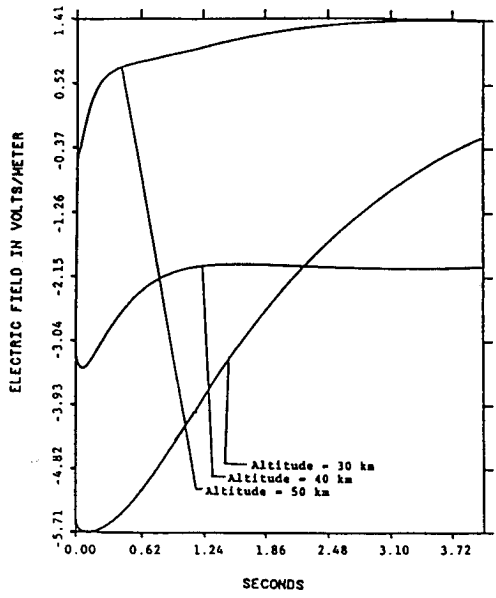

Figure 3.28 Vertical distribution of simulated electric fields at Z = 30 km for a dipole with (-) 10 km upper and (+) 6 km lower charge centers using real conductivity.

4. Comparison of Simulations and Measurements

Part of the motivation of this study was to simulate the electromagnetic scenario that was present during the Wallops Island, August 8, 1981 experiment [23]. The third conductivity profile (REAL) selected for the study was, as stated earlier, obtained primarily from this data (near-surface conductivity profile was extrapolated using Markson's [25] aircraft data). Therefore, simulations done using this conductivity (3.3.1 Dipole and 3.2.1 Monopole simulations) could be compared to the experimental electric field data. Since the relative position of the lightning with respect to the probe (rocket-borne payload containing nose-tip probe and Gerdien condenser) was unknown, the temporal structure, not the magnitude, was the focus of the investigation.

4.1 Description of the Experiment

The experiment was conducted on August 8, 1981, during a thunderstorm at Wallops Island, Virginia. The collected data shows lightning-related electric field waveforms that, for may cases, deviate significantly from a simple exponential time decay. All measurements

were taken at altitudes equal to or greater than 25.5 km. The specific waveforms selected for comparison are shown in Figs. 4.1–4.3. Figure 4.1 shows a vertical electric field waveform that was recorded at an altitude of 40 km. The waveform has two interesting features: 1) A polarity reversal that occurs approximately 4 seconds after the transient onset. 2) The tapering off of the electric field to a nearly constant value of 0.25 volts/meter.

Figure 4.2 shows an electric field waveform that was attained at an altitude of 47.5 km. The electric field remains strictly positive for the duration of the transient and shows again the asymptotic approach to a nearly constant non-zero value.

Figure 4.3 shows electric field schema (resulting from intracloud and cloud-to-ground lightning) obtained at altitudes of 25.5 km to 47.5 km. In both waveforms the maximum electric field value is delayed by 30 ms or more.

4.2 Comparison of the Waveforms

A careful study of the simulated electric field waveforms revealed that several of these closely resembled the temporal structure of the measured electric fields. What follows is the identification of the characteristics observed in the measurements and simulated by the computer model:

1) The polarity reversal and waveform shown in Fig. 4.1 (measurements) were approximated by the simulation shown in Fig. 3.20. Both of these waveforms are temporally quite similar; they tend to track one another fairly well.

2) The electric field behavior shown in Fig. 4.2 described and modeled by Hale [24] using a double exponential (i.e., the sum of two exponentially decaying terms with different time constants) was observed to some degree in all simulations. Figure 3.7 of the simulations bears the closest resemblance to this waveform.

3) The late-time gradual field recovery shown in Fig. 4.3 (altitude of 47.5 km) was simulated in Figure 3.9 (altitude of 50 km). Hale [24] attributed this phenomenon to "slow recharging" of the electric field (assuming Hale's statement implicitly indicates and active cloud charging current). However, since all forced charge perturbations have ceased (in the model) long before this behavior is observed in the simulated electric fields, it seems to be explainable in terms of a passive atmospheric response as well.

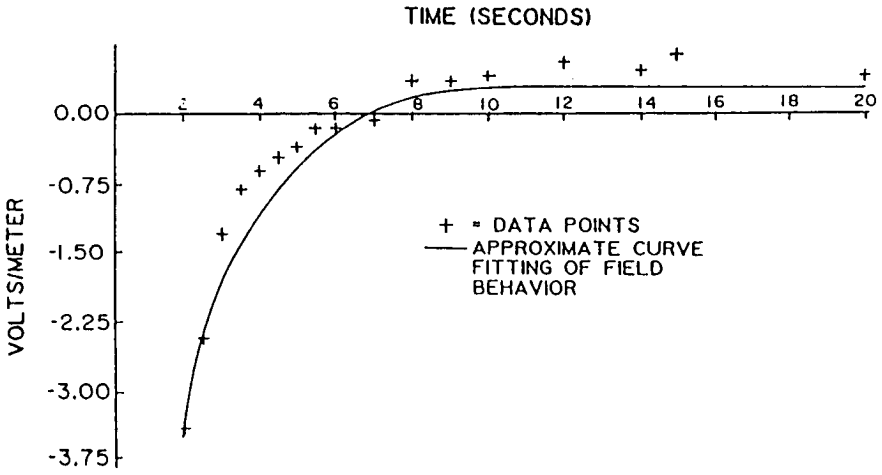

Figure 4.1 Electric fields measured at 40 km August 8, 1981 by L. C. Hale and C. L. Croskey. Presented at AGU Fall meeting, San Francisco, California, December 1989.

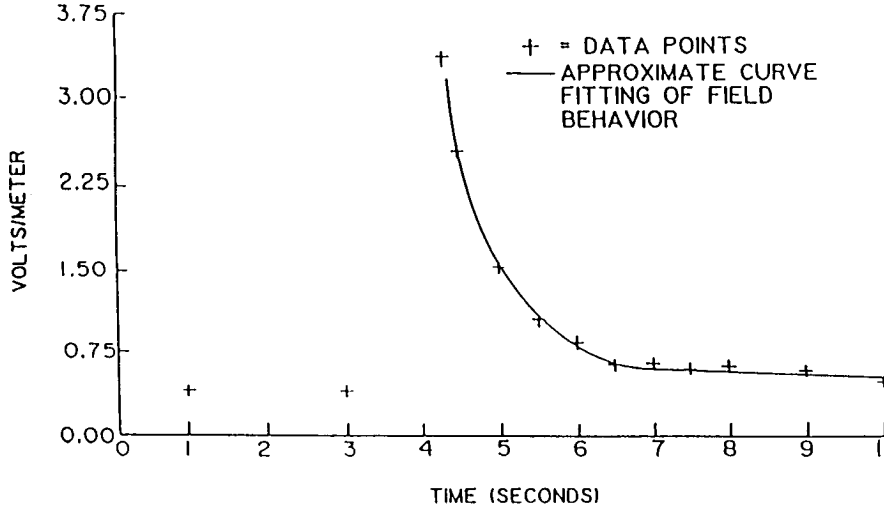

Figure 4.2 Electric fields measured at 47.5 km August 8, 1981 by L. C. Hale and C. L. Croskey. Presented at AGU Fall meeting, San Francisco, Califomia, December 1989.

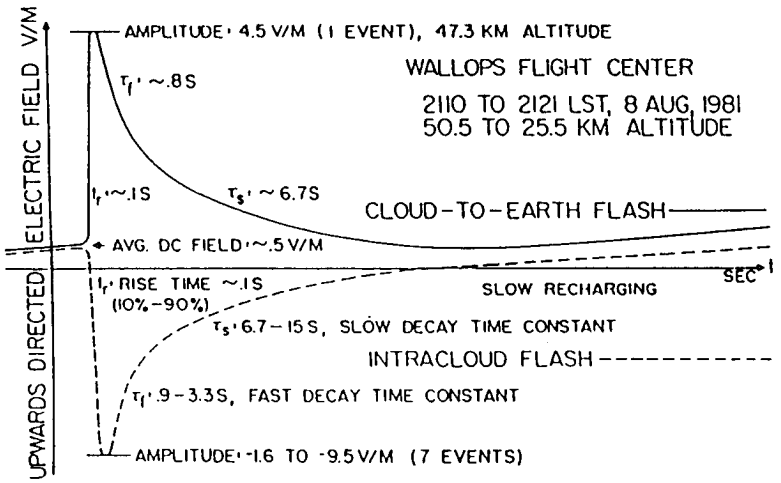

Figure 4.3 Electric fields measured at 47.3 km August 8, 1981 by L. C. Hale and C. L. Croskey. Presented at AGU Fall meeting, San Francisco, Califomia, December 1989.

5. Conclusions

5.1 The Results of the Study

Four conclusions my be drawn from this study:

1) The conservative electric field approximation, when used to analyze the atmosphere's transient electrodynamic response, will lead to solutions that are generally incorrect.

2) The late-time response (late-time $\langle T_1 \rangle$ is defined here as $T_1 > 3\tau(X)$, where $\tau = \epsilon_0/\sigma(\underline{x}), \underline{x}$ is the position where the simulation occurs) of the simulated electric field is relatively insensitive to the value of conductivity at the point where the simulations occur.

3) The temporal structure of the simulated electric field immediately following the onset of the initial maximum is approximately proportional to $\exp(-t/\tau(x))$ (defined above), i.e., $\exp(-t/T(x))$ follows or tracks the simulations for this time regime. The electric field simulations maintain this similarity for approximately $2\tau(X)$.

4) The amount of energy deposited in the atmosphere, based on the results of this study at altitudes of 40 km and above is much

greater than a conservative electric field model (assuming identical model parameters) would predict. This phenomenon, of relatively large energy deposition in the middle atmosphere and above, may explain in part the reported correlation of high-altitude electron precipitation to lightning events [18].

The conservative electric field assumption, if used, constrains the resulting electric field to decay exponentially in time (E will be proportional to $\exp(-t/\tau(\underline{x})$.

All vertical electric field simulations presented strongly deviate from the simple exponential decay (above premise). This deviation is most pronounced prior to the initial maximum and at late times. The evidence that suggests the second conclusion stated above can be briefly stated as follows:

—All vertical electric field simulations conducted at altitudes of 40 km and 50 km showed a large difference in the initial versus late-time rate of decay. The late-time behavior was, in all cases, relatively gradual compared to the initial decay following the peak (the maximum of the electric field waveform) and is relatively independent of altitude and of the conductivity at the position of the simulation.

The evidence that suggests the third conclusion requires a general inspection of all electric field simulation; therefore, no summary is presented.

The evidence that suggests the fourth conclusion can be briefly stated as follows:

—The electric field simulations (for all cases), at altitudes of 40 km or greater, showed a much longer temporal duration than could be explained if the conservative electric field assumption were assumed.

—The electromagnetic energy dissipated (joule heating) in a region of space is given by the integral:

$$\text{dissipated energy} = \int_0^a \int_{\text{region}} (\sigma \overline{E}^2 d_{\text{vol}}) dt$$

Therefore, the late-time duration of the electric fields (referred to as late-time tails by Holzworth and Chiu [5] greatly increase the total energy dissipated.

Appendix A: Computer Code

The partial differential equations describing the electrodynamic response of the atmosphere are developed into the exact form required by TWODEPEP for input data. The equations (2.10 and 2.11) are listed below:

$$\nabla\rho/\epsilon_0 = \nabla^2\overline{E} - \mu_0\sigma\partial\overline{E}/\partial t - \mu_0\epsilon_0\partial^2\overline{E}/\partial t^2 \tag{2.10}$$

$$0 = \sigma\rho/\epsilon_0 + \nabla\sigma\cdot\overline{E} + \partial\rho/\partial t + \overline{G}_s \tag{2.11}$$

where

$\overline{J}_s =$ source current inducing the charge perturbation

$\nabla\cdot\overline{J}_s = \overline{G}_s =$ source charge generator creating perturbation

Vertical (axial) symmetry is assumed in this study with spatial position being defined using a cylindrical coordinate system (r, ϕ, Z). The development proceeds as follows:

$$\begin{aligned}\nabla^2\overline{E} =&[\nabla^2 E_r - E_r/r^2 - 2(\partial E\phi/\partial\phi)/r^2]\overline{a}_r + \\ &[\nabla^2 - \phi - E_\phi/r^2 + s(\partial E_r/\partial\phi)/r^2]\overline{a}_\phi + \\ &[\nabla^2 E_z]\overline{a}_z\end{aligned}$$

where $\overline{a}(r, \phi, z)$ is a unit vector in the respective direction.

Axial symmetry eliminates all terms that vary with respect to, or are functions of, ϕ. The above equation therefore reduces to:

$$\nabla^2 E = [\nabla^2 E_r - E_r/r^2]\overline{a}_r + [\nabla^2 E_z]\overline{a}_z$$

where

$$\nabla^2 E_z = \partial^2 E_z/\partial z^2 + 1/r(\partial/\partial r(r\partial E_z/\partial z))$$

$$\nabla^2 E_r = \partial^2 E_r/\partial r^2 + 1/r(\partial/\partial r(r\partial E_r/\partial r))$$

Only the vertical component (a_z) of equation 2.10, in conjunction with equation 2.11, is required for a unique solution, via simulation, of the system (for linear systems, 2 equations with 2 unknows will have only one (1) unique solution; this is discussed at length in Chapter 3, [26]. A more detailed discussion of this specific development is given

by Holzworth and Chiu [5]. The variables simulated in the study are E_z and ρ and the equations are given as:

$$\mu_0\epsilon_0\partial^2 E_z/\partial t^2 = -\nabla\rho/\epsilon_0 + \nabla^2 E_z - \mu_0\sigma\partial E_z/\partial t$$
$$U = \partial E_z/\partial t, \quad V = E_z$$
$$\nabla^2 E_z = \partial(\partial E_z/\partial a)/\partial z + \partial(\partial E_z/\partial r)/\partial r)/\partial r)/\partial r + 1/r(\partial E_z/\partial r)$$
$$\nabla\rho = \partial\rho/\partial z, \quad \nabla\sigma = \partial\sigma/\partial z$$
in program: $r \rightarrow x$, $z \rightarrow y$, $\partial U/\partial x \rightarrow UX$
$\partial U/\partial y \rightarrow UY$, $\partial V/\partial x \rightarrow VX$, $\partial V/\partial y \rightarrow VY$
SET = 1
OXX = V
OXY = VY − USET(2)/8.854D − 12
F1 = VX/X − SIGMA (X, Y)*12.56637D − 7*U
C1 = 1.D0/9.D16
C2 = 1.D0
SET = 2
$-\partial\rho/\partial t = \sigma/\epsilon_0 + \nabla\sigma E_z + G_s$
$\nabla\sigma = \partial\sigma/\partial z$ = SIGMA$(X, Y)/FH(X, Y)$
$U = \rho$
C1 = −1.D0
F1 = SIGMA(X, Y)*$(U$/8.854D − 12 + VSET (1)/FH(x, y))
− GPH(x, Y, T)

Several excerpts from TWODEPEP's 5th Edition Manual, containing the most frequently referenced information, are listed as an aid, followed by the program. They contain definitions of the program variables and provide a brief overview of the software's operation and construction.

The boundary conditions are realized in the program using the ARC functions as follows:

$$\text{ARC} = +1 \text{ (vertical axis, } r = 0 \text{ km)}$$

When cylindrical symmetry is present, the vertical axis represents a line of symmetry. This condition requires that the value of all parameters tend to a local minimum or maximum in the limit as the vertical

axis is approached, i.e., $\lim_{r \to 0} = 0$ where F represents all program parameters.

$$\text{ARC} = +2, +4 \text{ (upper and lower boundaries)}$$

Both of these boundaries are modeled as perfectly conducting surfaces, and, as previously discussed, the radial component of the electric field at these boundaries becomes negligibly small ($E_r = 0$) in the limit as z approaches zero (lower boundary) or 80 km (upper boundary). Therefore, for these boundaries, $\nabla \cdot \overline{E} = \rho/\epsilon_0$ is expressible as $\partial E_z/\partial z = \rho/\epsilon_0$,

$$\text{i.e.,} \lim_{z \to 0 \text{ km, } 80 \text{ km}} (\nabla \cdot \overline{E}) = \partial E_z/\partial z = \rho/\epsilon_0$$

$$\text{ARC} = -3$$

The vertical electric field (E_z) and charge density (ρ) were assumed to be negligibly small at a radial distance of 60 km. It was found that simulations done using these conditions were insensitive to changes beyond 50 km. Therefore, selecting a 60 km radial limit is a measure taken to provide additional confidence in the simulations.

```
**** The vertical electric fields resulting from
**** charge perturbations located at either 6 km or 10 km
**** are simulated using TWODEPEP.
21 100 1
SET=1
**** Equation 2.10 is described using Fortran statements
**** in SET = 1.  The parameters of this SET are:
**** U=dE_z/dt, V=E_z.  The vertical component (a_z) of equation
**** 2.10 is solved for and formulated as follows:
**** The z-component of the vector laplacian + Del**2(E)
**** Del**2(E) = d/dz[d/dz(E_z)] + (1/r)d/dr[rd/dr(E_z)]
**** Del**2(E) = d/dz[d/dz(E_z)] + d/dr[d/dr(E_z)] +
****                (1/r)d/dr[E_z]
**** in the statements, r = x, z = y,
**** d/dr[d/dr(E_z)] = d/dx(OXX), OXX = d/dx(VX)
**** d/dz[d/dz(E_z)] - (1/8.854D-12)d/dz(Uset(2)) = d/dy(OXY)
**** OXY = VY - USET(2)/8.854D-12
**** F1 = (1/r)d/dr[E_z] - SIGMA(X,Y)[12.56637D-7][U]
C1          1.DO/9.D16
OXX          VX
OXY          VY-USET(2)/8.854D-12
NUDPT        3.DO
F1          (VX/X-SIGMA(X,Y)*12.56637D-7*U
**** UPRINT is used to reformat the output data file
UPRINT       V
C2          1.DO
F2          U
SET=2
**** Equation 2.11 is represented in Fortran statements
**** in this SET.  U = pho, the charge density
**** The GRAD(SIGMA) = SIGMA/FH(X,Y), which multiplies
**** VSET(1); (VSET(1) = E_z)
F1          SIGMA(X,Y)*(U/8.854D-12+VSET(1)/FH(X,Y))-GPH(X,Y,T)
C1         -1.DO
NUPDT        3.DO
NOUT         1
```

```
**** The value of 6.D3 in D3EST will be changed to 10.D3
**** for simulations done using the upper charge perturbation
D3EST       1.D0/SQRT(X*X+(Y-6.D3)**2+1.D-5)
**** UPRINT is used to reformat the output data file
UPRINT      V
NX          4.D0
NY          3.D0
HX         10.D3
HY         10.D3
TF          4.D0
DT          1.D-2
DTINV       1.D0/(T)**0.55
ALPHA       1.D0
YA          3.D4
XGRID       0.D0, 2.D3, 5.D3, 25.D3, 60.D3
YGRID       0.D0, 6.D3, 12.D3, 20.D3, 80.D3
IX         1,-3
IY         2,4
ADD.
**** One of the following conductivity profiles is selected
**** by deleting "****" in its first four (4) columns
**** When changing conductivities, it is important to replace
**** "****" in the first four columns of the previously
**** simulated conductivity.  Failure to do so will generate
**** an error
**** THE CONDUCTIVITY:
            FUNCTION SIGMA(X,Y)
**** EXPONENTIAL CONDUCTIVITY
****        SIGMA=5.D-14*EXP(Y/6.D+3)
            IF (Y.LT.4.D3) F1=2.94D0/EXP(4.5D-3*Y)
            IF (Y.GE.4.D3) F1=0.D0
            F3=0.369D0/EXP(1.21D-4*Y)
            F2=1.39D0/EXP(3.75D-4*Y)
**** GISH CONDUCTIVITY
****        SIGMA=1.D-13/(F1+F2+F3)
            IF(Y.LT.5.D3) F5=9.D0/EXP(Y/360.D0)
            IF(Y.GE.5.D3) F5=0.D0
```

```
            F4=0.369D0/EXP(Y/7700.D0)
**** REAL CONDUCTIVITY
****        SIGMA=6.D-14/(F1+F2+F4+F5)
             RETURN
             END
**** The function GPH(X,Y,T) is the charge perturbation
**** in terms of Fortran statements.  The user-supplied
**** terms are defined as follows:
**** SD = usually defined as the standard deviation, controls
****      the charge perturbation's radial profile
**** DQ = amount of total charge generated during the
****      charge perturbation
**** YO = vertical location of the charge perturbation
****  V = in this subroutine, V is defined as the variance
****      (not used as a user-supplied term in this routine)
**** THE CHARGE PERTURBATION:
**** T1 = decay or fall time of the charge perturbation
            FUNCTION GPH(X,Y,T)
            SD=3.D3
            DQ=1.D+0
            YO=6.D+3
            V=SD*SD
            DR=X*X+(Y-YO)**2.D0
            IF(DR.LT.63.D6) BAR=EXP(-DR/(2.D0*V))
            IF(DR.GE.63.D6) BAR=0.D0
            T1=1.D-4
            AUG=T/T1
**** The use of the exponential operator requires arguments
**** that are within the range: -30.0 < argument < 30.0
            IF(AUG.LT.30.D0) ER=EXP(-AUG)
            IF(AUG.GE.30.D0) ER=0.D0
**** PHO = spatial structure of charge perturbation
**** ER/t1 = sets the total amount of charge exchanged to
****          be independent of the value of T1
           PHO=DQ/(2.D0*V*3.14159D0)**1.5*BAR
**** The total charge contained within the spatial
**** distribution of PHO is found by integrating PHO over the volume
****
****        TOTAL CHARGE = ∫_0^a PHO(R')*(4.*3.14159*R'*R')dR'
****
```

```
****                    = 1.D0
****        where       a = infinity
****                    R' = SQRT(X*X+(Y-Y0)**2.)
****                    Y0 = is altitude of charge
****                         perturbation
****                    PHO is converted to spherical
****                         coordinates
****                         The integral and solution are
****                         found on page 307 of TABLE OF
****                         INTEGRALS, SERIES, AND PRODUCTS,
****                         Gradshteyn and Ryzhik, 1980
            GPH =PHO*ER/T1
            RETURN
            END
**** FH(X,Y) is used to define the gradient of the
**** conductivity that appears in equation 2.11.
**** Each of the three conductivities require a separate
**** form of FH(X,Y) shown below.  Changing the value of
**** FH(X,Y) is done using the same procedure as described
**** for the conductivity
            FUNCTION FH(X,Y)
            IF(Y.LT.4.D3) F1=2.94D0/EXP(4.5D-3*Y)
            IF(Y.GE.4.D3) F1=0.D0
            F3=0.369D0/EXP(1.21D-4*Y)
            F2=1.39D0/EXP(3.75D-4*Y)
            GISH=1.D-13/(F1+F2+F3)
**** FH FOR EXPONENTIAL CONDUCTIVITY
****        FH=6.D3

**** FH FOR GISH CONDUCTIVITY
****        FH=1.D-13/((4.5D-3*F1+3.75D-4*F2+1.21D-4*F3)*GISH)
            IF(Y.LT.5.D3) F5=(9.D0/EXP(Y/360.D0))
            IF(Y.GE.5000.D0)F5=0.D0
            F4=0.369D0/EXP(Y/7700.D0)
            SIGMA3=6.D-14/(F1+F2+F4+F5)
**** FH FOR REAL CONDUCTIVITY
****        FH=6.D-14/(SIGMA3*(4.5D-3*F1+3.75D-4*F2+F4/7700.D0
                                +F5/360.D0))
            RETURN
            END
END.
```

References

1. Wilson, C. T. R., "Some thundercloud problems," *J. Franklin Inst.,* Vol. 208, 1916.
2. Watson, R. A., and J. Craib, "The electric field of South African thunderstorms," *Proc. R. Soc.,* Ser. A, Vol. 114, 229–243, 1920.
3. Appleton, E. V., R. A. Watson-Watt, and J. F. Herd, "On the nature of the atmosphere," *Proc. Roy. Soc.,* Vol. A 111, 654, 1926.
4. Israel, H., *Atmospheric Electricity, Israel Program for Scientific Translations,* Vol. 2, Jerusalem, 1973.
5. Holzworth, R. H., and Y. T. Chiu, "Spherics in the stratosphere," In *CRC Handbook of Atmospherics,* Volume one, H. Volland, CRC Press, Boca Raton, Florida, 65, 1982.
6. Uman, M. A., *Lightning,* McGraw-Hill, New York, 1969.
7. Gish, O. H., "Evaluation and interpolation of the columnar resistance of the atmosphere," *Terr. Magn. Atmos. Electr.,* Vol. 99, 159–168.
8. Golde, R. H., *Lighting,* Volume I, Academic Press, 1977.
9. Volland, H., *Atmospheric Electrodynamics Chemistry in Space,* Vol. II, Springer-Verlag, Berlin, Germany, 1984.
10. Tamure, Y., "An analysis of the electric field after lightning discharges," *Geophys. Res. Pap.,* Vol. 41, 190–200, 1955.
11. Kasemir, H. W., "The thunderstorm as a generator in the global electric circuit (in German)," *Z. Geophys.,* Vol. 25, 33, 1959.
12. Anderson, F. G., and G. D. Freier, "Interaction of the thunderstorm with a conducting atmosphere," *J. Geophys. Res.,* Vol. 74, 5390, 1969.
13. Illingworth, A. J., "Electric field recovery after lightning as the response of a conducting atmosphere to a field change," *Quart. J. Roy. Meteorol. Soc.,* Vol. 98, 604, 1972.
14. Park, C. G., and M. Dejnakarintra, "Penetration of thundercloud electric fields into the ionosphere and magnetosphere 1, Middle and subauroral latitudes," *J. Geophys. Res.,* Vol. 78, 6623–6633, 1973.
15. Greifinger, C., and P. Greifinger, "Transient ULF electric and magnetic fields following a lightning discharge," *J. Geophys. Res.,* Vol. 81, 2237, 1976.
16. Nisbet, J. S., "A dynamic model of thundercloud electric fields," *J. Atmos. Sci.,* Vol. 40, 2855, 1983.

17. Baginski, M. E., L. C. Hale, and J. J. Olivero, "Lightning-related fields in the ionosphere," *Geophysical Res. Let.,* Vol. 15. No. 8, 764–767, August 1988
18. Hale, L. C., and M. E. Baginski, "Current to the ionosphere following a lightning stroke," *Nature,* Vol. 329, No. 6142, 814–816, 29 Oct., 1987
19. Sunde, E. D., *Earth Conduction Effects in Transmission Systems,* Dover, New York, 1968.
20. Baum, C. E. "Simulation of electromagnetic aspects of lightning," *Proc. of Lightning Tech.,* NASA Conf. Pub. 2128, April 1980.
21. Baginski, M. E., "Finite element simulation of the atmosphere's electromagnetic response to charge perturbations associated with lightning," Ph.D. thesis, The Pennsylvania State University, 111, 1987.
22. Stratton, J. A., *Electromagnetic Theory,* McGraw-Hill, New York, 1941.
23. Holzworth, R. H., M. C. Kelly, C. L. Siefring, L. C. Hale, and J. D. Mitchell, "Electrical measurements in the atmosphere and ionosphere over an active thunderstorm: 2. Electric field and conductivity," *J. Geophys. Res.,* Vol. 90, 9824–9830, 1985.
24. Hale, L. C., "Middle atmosphere electrical structure, dynamics, and coupling," *Adv. Space Res.,* Vol. 4, 175–186, 1984.
25. Markson, R., and L. C. Hale, "Electrical measurements in the atmosphere and ionosphere over an active thunderstorm," presented at AGU Meeting, Philadelphia, Pennsylvania, 1982.
26. Berkey, G. A., and W. J. Karplus, *Hybrid Computation,* Volume one, Wiley, 1968.
27. Malan, D. J., "The distribution of electricity in thunderclouds," *Proc. R. Soc.,* Ser. A., Vol. 209, 177, 1958.
28. I.M.S.L. *TWODEPEP.,* 5th Edition, Dallas Texas, 1985.

List of Symbols

Quantity	Symbol	Unit
Charge	q or $\overline{Q}$	coulomb
Current	i or $\overline{I}$	ampere
Charge Density	ρ	coulomb/meter^3
Current density	$\overline{J}$	ampere/meter^3
Conductivity	σ	mho/meter
Electric field intensity	$\overline{E}$	volt/meter
Electric potential	ϕ	volt
Dielectric displacement	$\overline{D}$	coulomb/meter^2
Inductive capacity of free space	ϵ_0	farad/meter
Magnetic Flux	Φ	weber
Magnetic flux density	$\overline{B}$	weber/meter^3
Magnetic field intensity	$\overline{H}$	ampere-turn/meter
permeability of free space	μ_0	henry/meter